RSC Advances

PAPER

View Article Online
View Journal | View Issue

Cite this: *RSC Adv.*, 2025, **15**, 1072

Mechanistic study of the adsorption capabilities of heavy metals on the surface of ferrihydrite: batch sorption, modeling, and density functional theory†

Bihong He,[a] Wentao Zhang,[*b] Yanan Diao,[c] Shangchen Sun,[a] Yonghe Zhang,[a] Wenqing Zhao,[a] Fei Wen[a] and Guangrui Yang[d]

Ferrihydrite (Fh), a widely distributed mineral in the environment, plays a crucial role in the geochemical cycling of elements. This study used experimental and computational approaches to investigate the adsorption behavior of seven heavy metal ions on Fh. The pH edge analysis revealed that the adsorption capacity followed the order: Pb^{2+} > Cu^{2+} > Zn^{2+} > Cd^{2+} > Ni^{2+} > Co^{2+} > Mn^{2+}, with Pb^{2+} showed the highest adsorption. Competitive adsorption was observed in multi-metal systems, and adsorption isotherms confirmed that Pb^{2+} and Cu^{2+} exhibited significantly higher equilibrium adsorption capacities than the other ions. Diffuse Layer Model (DLM) analysis indicated that for most heavy metals (HMs), ≡Fe^{s}OM and ≡Fe^{w}OM were the predominant adsorption species, while for Pb^{2+}, ≡Fe^{s}OPb dominated. Density Functional Theory (DFT) calculations were employed further to investigate the molecular interactions between HMs and Fh. The DFT results revealed that the distribution of surface iron sites on Fh strongly influences the adsorption process. Larger metal ions, such as Pb^{2+}, form stronger coordination bonds with hydroxyl groups on the Fh surface, leading to distinct adsorption mechanisms compared to smaller ions. These findings, combining experimental and computational data, emphasize the critical role of surface iron site distribution and ion size in governing the adsorption behavior of HMs on Fh.

Received 16th October 2024
Accepted 3rd January 2025

DOI: 10.1039/d4ra07426b

rsc.li/rsc-advances

1. Introduction

Mining, smelting, fossil fuel combustion, and other human activities may release large amounts of heavy metals (HMs) into the environment, leading to excessive accumulation of HMs in the surrounding environmental media.[1–10] Related studies have shown that ecological media such as water, atmosphere, and soil play a crucial role in the migration, transformation, and cycling of HMs on Earth.[11–14] HMs in water and atmosphere can enter the soil through various pathways, leading to excessive accumulation of HMs.[15,16] Through the food chain, HMs in these environmental media will inevitably enter the human body through direct and indirect pathways and undergo enrichment, thereby causing significant harm to human health and the ecological environment.[17–20] Taking Cd as an example, even chronic and low levels of cadmium exposure can lead to a series of diseases in the human body, such as cardiovascular and kidney diseases, cancer, osteoporosis, bone deformation, *etc.*[21–24] In addition, excessive Pb in children's bodies may cause irreversible damage to their nervous system, leading to intellectual problems.[25] Although Zn, Cu, and Cr are essential for life activities, they can still exhibit high toxicity at high concentrations.[26]

Ferrihydrite (Fh) is a reddish-brown spherical nanoparticle widely distributed in water, soil, sediment, and organisms. The flotation process of sulfide ore produces acidic iron sulfate wastewater, which can easily form Fh after neutralization. Fh is also a common product of steel corrosion. According to the XRD spectrum, 2 line-Fh and 6 line-Fh are the main structures, and the 2 line-Fh is the main form in the environment, which received high attention. Due to its large specific surface area and high surface activity, Fh has become an important adsorbent for various trace elements that affect the form, migration, and transformation of polluting and nutrient elements through complex interactions in environments such as rocks, sediments, soil, water, atmosphere, and organisms, and plays a critical role in the geochemical cycling of elements.[27]

In environmental media, HMs often do not exist alone, but rather coexistence, especially in mining and smelting. These ions will compete for adsorption sites, affecting their respective adsorption efficiency and behavior. Numerous studies have shown that the enrichment ability of typical heavy metal (HM)

[a]*Yellow River Basin Ecotope Integration of Industry and Education Research Institute, Lanzhou Resources & Environment Voc-Tech University, Lanzhou, 730000, China*
[b]*Northwest Institute of Eco-Environment and Resources, Chinese Academy of Sciences, Lanzhou 730000, China. E-mail: gslzwtao@sina.com*
[c]*School of Chemistry, State Key Laboratory of Fine Chemicals, Dalian University of Technology, Dalian, 116024, China*
[d]*Gansu Zhongshang Food Quality Test and Detection Co., Ltd, Lanzhou, 730010, China*

† Electronic supplementary information (ESI) available. See DOI: https://doi.org/10.1039/d4ra07426b

ions (Pb^{2+}, Cu^{2+}, Zn^{2+}, Cd^{2+}, Ni^{2+}, Co^{2+}, and Mn^{2+}) in environmental media on the surface of Fh varies significantly,[28–30] and the reason is a question worth exploring. Studying the adsorption mechanism of HM ions on the surface of Fh is significant for explaining the migration and transformation behavior of HMs in the environment and controlling pollutants. It is generally believed that the adsorption capacity of HMs on mineral surfaces is mainly related to their charge density and hydrolysis constant,[31,32] but this statement is not accurate enough. The adsorption behavior of HMs is often studied using Langmuir and Freundlich adsorption isotherm models to somewhat reflect the adsorption capacity. However, these models cannot reflect the surface adsorption characteristics of minerals and explain the adsorption mechanism of HMs well. The surface complexation modeling established based on surface complexation and chemical equilibrium theory fully considers information related to surface adsorption behavior, such as active sites, adsorption forms, and complexation constants, making it a favorable tool for simulating and predicting the adsorption process of HMs in complex systems.[33–36] Besides, the different adsorption abilities of HMs on mineral surfaces may be related to the outer electron arrangement of these HMs. Taking the adsorption of typical HM ions (Pb^{2+}, Cu^{2+}, Zn^{2+}, Cd^{2+}, Ni^{2+}, Co^{2+}, and Mn^{2+}) on the surface of Fh in environmental media as an example, Pb^{2+} is the leading group element, with a peripheral electron layer arrangement of $6s^26p^2$. At the same time, Cu^{2+}, Zn^{2+}, Cd^{2+}, Ni^{2+}, Co^{2+}, and Mn^{2+} are all transition elements, with the valence electron configuration of $(n-1)\,d^{1-9}\,ns$.[1,2] To further explore the mechanism underlying the different adsorption capabilities of HMs on the surface of Fh, Density Functional Theory (DFT), a quantum mechanical method used to study the electronic structure of multi-electron systems,[37,38] may be a powerful tool to elucidate it.

This study investigates the differential enrichment mechanisms of typical HM ions on the Fh surface in environmental media, using batch experiments, surface complexation models, and DFT calculations. X-ray diffraction (XRD) analysis identified low-index surfaces, including the (103), (112), and (201) planes, which were then examined for their interfacial properties through DFT calculations for the first time. DFT calculations were further employed to assess the variation in HM cation adsorption across different iron-exposed facets of Fh. This combined approach offers a novel perspective on the adsorption order of HM ions on the Fh surface. Understanding the adsorption mechanisms of HMs on Fh is crucial for accurately assessing ecological risks associated with HM contamination and for the development of more effective pollution prevention strategies, thus providing a scientific basis for environmental protection policies.

2 Materials and methods

2.1 Synthesis of the 2-line Fh

The 2-line Fh was synthesized following the method reported by Schwertmann U. and Cornell R. M.[39] Typically, 8.0 g $Fe(NO_3)_3\cdot 9H_2O$ was weighed and dissolved in 100 mL of water, then 1.0 mol L^{-1} KOH about 66 mL was dropped in the $Fe(NO_3)_3$ solution under magnetic stirring and the pH was adjusted to 7–8. The resulting suspension was allowed to stand, the supernatant was discarded, and the obtained solid was rinsed with water. This operation was repeated 6–8 times, and finally, the resulting solids were freeze-dried, ground, and passed through a 200-mesh sieve. The specific surface area measured by nitrogen Brunauer–Emmett–Teller Analysis (N_2-BET) was 315 $m^2\ g^{-1}$.

2.2 Characterization

The X-ray diffraction (XRD) analysis of the Fh was performed on an X-ray diffractometer (XD-3A, Shimadzu, Japan) with Bragg–Brentano geometry for 2θ values in a range of 5–90°.

2.3 The sorption edges

The sorption pH edges were conducted with 5.0 g L^{-1} Fh and 1.0 mmol L^{-1} HMs solutions at $T = 25 \pm 1$ °C in the presence of 0.01 mol L^{-1} NaCl background electrolyte solution in both single and competitive systems. Establishing a competitive system can help us simulate this complex real-world environment, making the experimental results more representative and meaningful in practice and contributing to further investigating the adsorption mechanism of HM ions on the surface of adsorbents. This study established the competition system with the coexistence of 7 typical HM ions (Pb^{2+}, Cu^{2+}, Zn^{2+}, Cd^{2+}, Ni^{2+}, Co^{2+}, and Mn^{2+}). The concentrations of HM ions in the separated liquids were measured by an *n* inductively coupled plasma optical emission spectrometer (ICP-OES, PerkinElmer, Optima 8000). The adsorption percentage of HM ions on Fh was calculated by the formula (1), in which C_0 (mol L^{-1}) and C_{eq} (mol L^{-1}) were the initial and equilibrium concentrations of HM ions, respectively.

$$\text{Adsorption}\ (\%) = \frac{C_0 - C_{eq}}{C_0} \times 100\% \quad (1)$$

2.4 The sorption isotherms

0.03 g 2-line Fh and about 1 mL background electrolyte solution (NaCl, 0.1 mol L^{-1}) were added into a series of 10 mL polyethylene centrifuge tubes. After 24 hours of pre-equilibrate, sequentially added different volumes of a mixed solution containing 7 HM ions and background electrolyte solution, making the total volume was 6.0 mL, solid–liquid ratio was 5.0 g L^{-1}, and background electrolyte concentration 0.01 mol L^{-1}. The pH of these samples was adjusted to 5.6 ± 0.1 using small amounts of HCl or NaOH. Then samples were placed in a constant temperature oscillator at 25 °C to oscillate, and the pH was maintained at 5.6 ± 0.1 throughout the equilibrium period by periodic adjustments. After the equilibrium was reached, the samples were centrifuged to separate the solid Fh from the supernatant. The equilibrium adsorption capacity of the HM ions on Fh was calculated using the following formula:

$$Q_e\ (\%) = \frac{(C_0 - C_e)}{m/v} \times 100\% \quad (2)$$

where C_0 and C_e are the initial and equilibrium concentrations of HM ions in the solution (mol L^{-1}), respectively, and m/v is the mass-to-volume ratio (g L^{-1}).

2.5 Surface complexation modeling

The diffuse double-layer surface complexation model (DLM) can effectively describe the electrostatic interactions between solid surface charges and ions in the solution, which is an essential factor affecting the adsorption behavior of HMs on the surface of Fh. In addition, the adsorption behavior of HMs on the surface of Fh involves multiple mechanisms, including electrostatic attraction, chemical complexation, surface precipitation, *etc.* The DLM can comprehensively consider these mechanisms and provide a more comprehensive and accurate description. To explore the sorption species and mechanism of HMs on Fh, the adsorption edges data were modeled by MINTEQ 3.1 Code[40] using a 2-site DLM which has hydroxyl sites with varying strong and weak charges developed by Dzombak and Morel. The $\equiv Fe^{s}OH$ represents the strong hydroxyl site, and the $\equiv Fe^{w}OH$ represents the weak hydroxyl site. Protonation and deprotonation reactions can occur on the surface of Fh, which can then react with HM ions as follows (M^{2+} represents HM ions):

$$\equiv Fe^{s}OH + M^{2+} \leftrightarrow \equiv Fe^{s}OM^{+} + H^{+} \quad (3)$$

$$\equiv Fe^{w}OH + M^{2+} \leftrightarrow \equiv Fe^{w}OM^{+} + H^{+} \quad (4)$$

$$\equiv Fe^{s}OM^{+} + H_2O \leftrightarrow \equiv Fe^{s}OMOH^{0} + H^{+} \quad (5)$$

$$\equiv Fe^{w}OM^{+} + H_2O \leftrightarrow \equiv Fe^{w}OMOH^{0} + H^{+} \quad (6)$$

2.6 Details of computational calculations

2.6.1 DFT parameters. All the DFT calculations were performed using the Vienna *Ab initio* Simulation Package (VASP),[41] and the Perdew–Burke–Ernzerhof (PBE)[42] potential was used as the gradient-corrected exchange–correlation functional. The projector augmented wave (PAW) method described the electron–ion interactions.[43] The energy cutoff for the plane wave basis expansion was set to 400 eV, and the force on each atom was less than 0.03 eV $Å^{-1}$ for the convergence criterion of the geometry relaxation. The self-consistent calculations were set to 10^{-5} eV as a convergence energy threshold. The *k*-points mesh was set to 2 × 2 × 1 for the unit cell and surface slabs for structure optimization, respectively. Furthermore, the van der Waals interaction was evaluated by a DFT-D3 method.[44] The correlation energy of the 3d orbital of Fe was described using the Hubbard U correction (DFT+U), and the effective single parameter U–J was set to 5.67 eV.[45] The DFT+U correction was employed to address the limitations of standard DFT in accurately describing the localized 3d electrons of transition metals, such as Fe, in Fh. Conventional DFT tends to underestimate the electronic correlation effects in Fe-containing systems, leading to inaccuracies in electronic structure and adsorption properties. By introducing the Hubbard U parameter, we achieved a more accurate representation of the localized Fe 3d states, which is critical for simulating the adsorption behavior of HM ions. The adsorption energy (E_{ads}) is defined using eqn (7).

$$E_{ads} = E_{slab+cation} - (E_{slab} + E_{cation}) \quad (7)$$

where $E_{slab+cation}$ is the total energy of the surface with cation adsorbed, E_{slab} and E_{cation} represent the energy of the bare surface and cation, respectively.

2.6.2 Calculations model. The structure of Fh used in this study belongs to the $P6_3mc$ space group, with the optimized lattice parameters $a = b = 5.96$ Å and $c = 8.97$ Å, and is classified as the 2-line type of Fh.[37] Based on the X-ray diffraction patterns of Fh, the low-index (103), (112), and (201) surfaces were cleavaged. The three-layered 1 × 2 supercells were constructed for the (103), (112), and (201) facets. The surface slab model consisted of 169 atoms.

A vacuum region of 15 Å was introduced along the *z*-axis to eliminate artificial interactions between periodic images under periodic boundary conditions, ensuring the accuracy of the calculations. In addition, the topmost two layers were relaxed during the energy optimization, while the bottommost layer was kept fixed to simulate the bulk. The charge distributions were calculated using the Bader charge method.[46] Bader charge analysis determined the electronic charge distribution of adsorbed ions (Pb^{2+}, Zn^{2+}, Ni^{2+}) on the Fh surface. It is important to note that the Bader charges are influenced by the local coordination environments of the ions and may differ from their charges in bulk materials, such as ZnO or PbO, due to the unique atomic arrangement and electron redistribution at the surface.

3 Results and discussion

3.1 Characterization of Fh

To further investigate the adsorption forms and mechanisms of Pb^{2+}, Cu^{2+}, Zn^{2+}, Cd^{2+}, Ni^{2+}, Co^{2+}, and Mn^{2+} on the surface of Fh, the 2-line Fh, which is widely present in soil and sediment environments, was prepared. The XRD pattern of the Fh was shown in Fig. 1, confirming that the synthesized material was 2-line Fh. The characteristic peaks at 31.1°, 35.3°, and 36.6° correspond to (103), (112), and (201) planes, respectively, of a hexagonal Fe(OH) (PDF #97-019-2677). The term 'PDF #97-019-2677' refers to the Powder Diffraction File database maintained by the International Centre for Diffraction Data (ICDD). This entry corresponds to the reference diffraction pattern for hexagonal $Fe(OH)_3$, which was used to identify the characteristic peaks of the synthesized Fh. Specifically, the diffraction peaks corresponding to these facets, observed at 31.1°, 35.3°, and 36.6°, exhibited significantly higher intensities compared to other potential planes, indicating that these facets are the most prevalent in our sample under the specific synthesis conditions used. While facets such as (100) and (111) are often considered "natural" in other crystalline materials and have been studied previously, they were not the focus of our work because they were either absent or displayed much lower intensities in the XRD pattern of our material, suggesting that they are less exposed. The structural characteristics of 2-line Fh, including its high degree of disorder and nanocrystalline nature, combined with the synthesis conditions, likely favor the kinetic stabilization and exposure of the (103), (112), and (201)

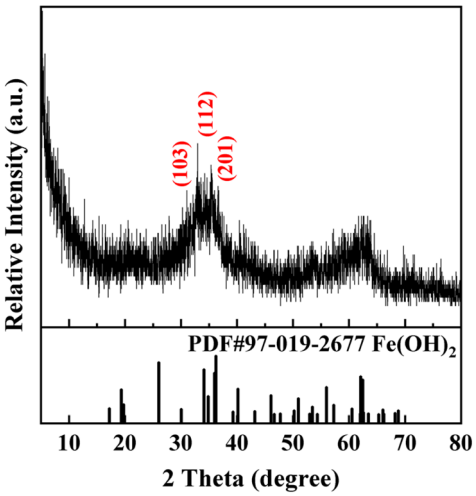

Fig. 1 Comparison between the experimental XRD pattern of the synthesized Fh and the theoretical XRD pattern obtained from the PDF database (ICDD).

facets over the (100) and (111) facets. Investigating these dominant facets is crucial as they are most likely to control the synthesized Fh's surface reactivity and interfacial chemical behavior.

3.2 Effect of pH

The effect of pH on the adsorption of HMs on the surface of Fh was investigated by batch experiment. As shown in Fig. 2, in both single and competitive systems, the adsorption percentage of these HMs on Fh increased as the pH increased from 3 to 8, with the maximum adsorption percentage of Pb reaching first at pH around 5. Generally, the lower the pH value, the greater the displacement of the adsorption edge of HMs, and the greater the affinity of HMs adsorbed on Fh. When the adsorption percentage of these HMs on Fh in a single system reached 50%, the pH from low to high was: 3.33 (Pb^{2+}), 4.76 (Cu^{2+}), 5.88 (Zn^{2+}), 6.04 (Cd^{2+}), 6.49 (Ni^{2+}), 6.56 (Co^{2+}) and 6.64 (Mn^{2+}), indicating that the adsorption capacity of HMs on Fh surface followed the following order: $Pb^{2+} > Cu^{2+} > Zn^{2+} > Cd^{2+} > Ni^{2+} > Co^{2+} > Mn^{2+}$. In the coexisting competition system, there was no significant change in the pH sorption edge of these HMs (Fig. 2(b)).

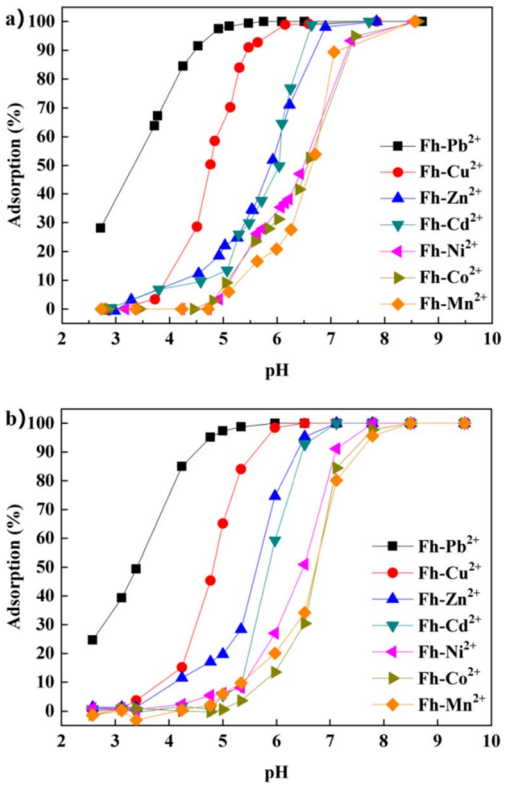

Fig. 2 Effects of pH on the sorption of 7 HMs on Fh in single (a) and competitive (b) system (mass-to-volume (m/v) = 5.0 g L^{-1}, I = 0.01 mol L^{-1} NaCl, T = 25 °C, $C_M = 1.0 \times 10^{-3}$ mol L^{-1}).

3.3 Adsorption isotherm

To compare the differences in the adsorption capacity of these HMs, the adsorption isotherms in both mono- and multi-systems at 25 °C were studied. As shown in Fig. 3, under the condition of pH = 5.6 ± 0.1 (m/v = 5.0 g L^{-1}, I = 0.01 mol L^{-1} NaCl), the equilibrium adsorption capacity adsorption capacities (mmol g^{-1}) of Pb^{2+}, Cu^{2+}, Zn^{2+}, Cd^{2+}, Ni^{2+}, Co^{2+}, and Mn^{2+} on the surface of Fh in the mono-system were 1.20, 0.62, 0.08, 0.047, 0.038, 0.036 and 0.027, respectively. The equilibrium adsorption capacity of Pb^{2+} and Cu^{2+} were much higher than the other five HMs, indicating that these two ions have a higher affinity on the surface of Fh. Moreover, compared with mono-systems, the equilibrium adsorption capacities (mmol g^{-1}) of Pb^{2+}, Cu^{2+}, Zn^{2+}, Cd^{2+}, Ni^{2+}, Co^{2+} and Mn^{2+} in multi-system have decreased, with values of 0.095, 0.235, 0.038, 0.028, 0.013, 0.012 and 0.020, respectively, and the percentage decrease reached 20.8%, 62.1%, 52.5%, 40.4%, 65.8%, 66.7% and 25.9%, respectively, indicating that there was a competitive effect of HMs on the surface of Fh in the multi-system. The equilibrium adsorption capacity of Pb^{2+} and Cu^{2+} was still much higher than the other five HMs. However, in both mono- and multi-systems, the order of the equilibrium adsorption capacity on the surface of Fh was the same as $Pb^{2+} > Cu^{2+} \gg Zn^{2+} > Cd^{2+} > Ni^{2+}$, Co^{2+}, and Mn^{2+}, further indicating that compared to other HMs, Pb^{2+}, and Cu^{2+} had a stronger affinity with the surface of Fh.

3.4 Surface complexation modeling

The fitting by the DLM was performed on the adsorption of HMs on the surface of Fh in the mono-system using MINTEQ 3.1 Code, which provided the parameters describing HM's adsorption on Fh. Based on the adsorption edges and the metal ion morphology calculation results in MINTEQ 3.1, no precipitation phase was generated in this experimental system. Except for Mn^{2+}, which does not have a hydrolytic state, the hydrolytic state contribution of the other six HM ions was almost none. As shown in Fig. 4, according to the fitting results, the system mainly undergo (3) and (4) reactions, and the contribution of (5) and (6) reactions were very small and could be ignored. The adsorption edges could be well fitted using the DLM, and the

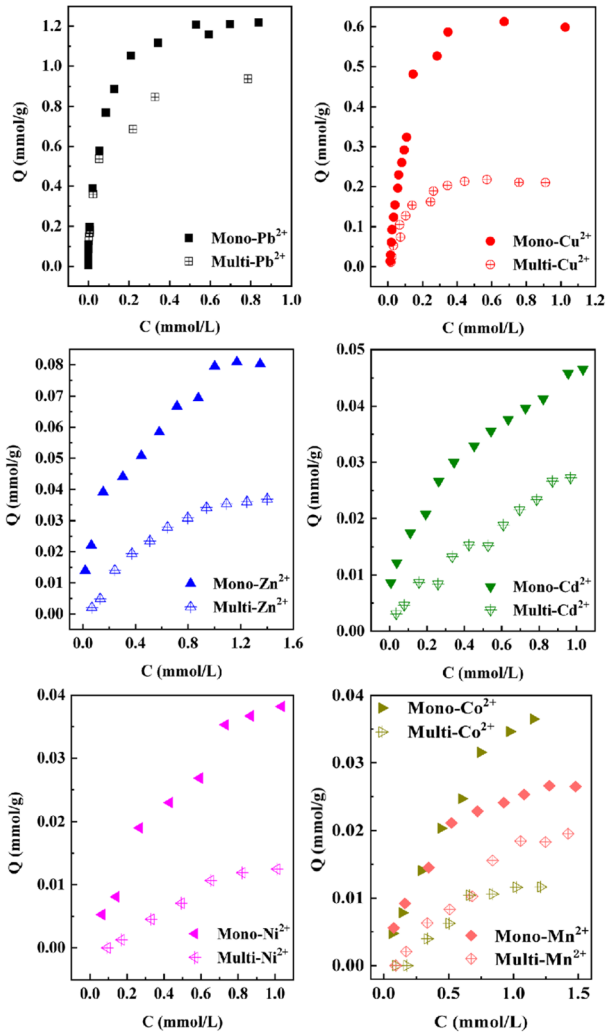

Fig. 3 Sorption isotherms of HMs (II) on Fh in mono- and multi-system (m/v = 5.0 g L^{-1}, I = 0.01 mol L^{-1} NaCl, T = 25 °C, pH = 5.6 ± 0.1).

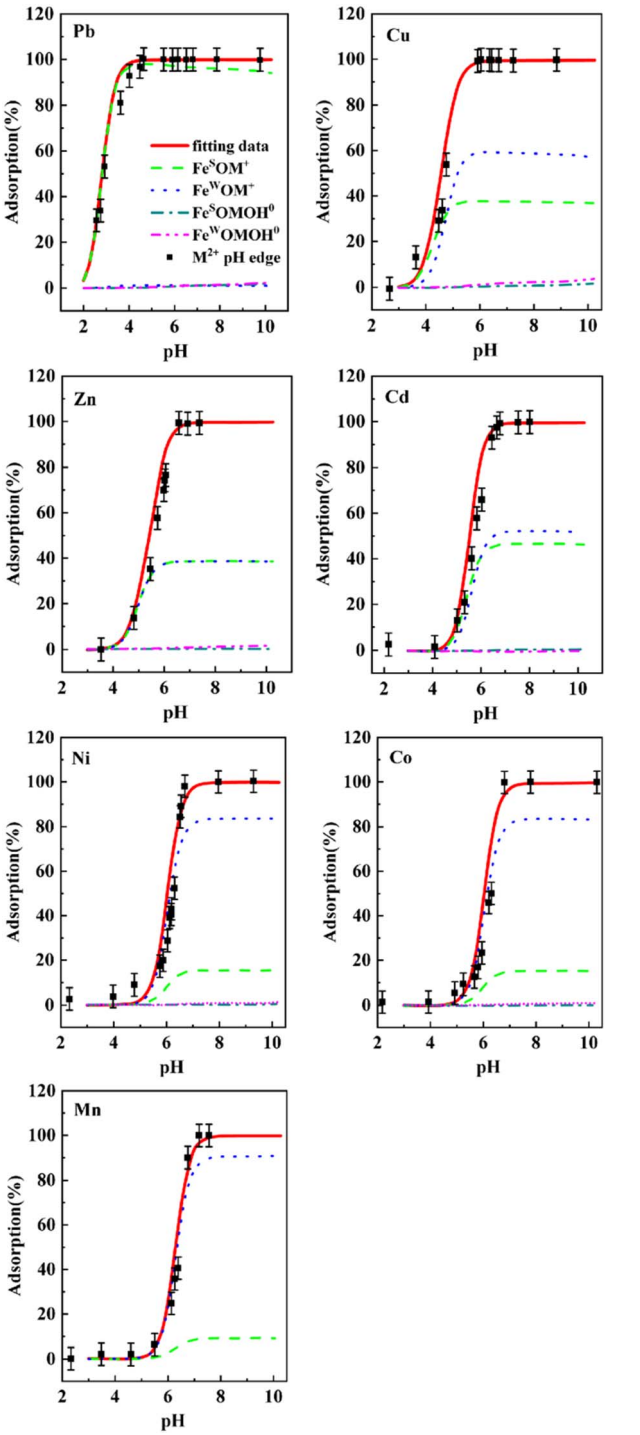

Fig. 4 Sorption and modeling of HMs on Fh as a function of pH (M represents metals).

fitted log K value was relatively close to previous research results (Table 1).[33–36] For Pb^{2+}, $\equiv Fe^{S}OPb^{+}$ was the main adsorption form, and the contribution of $\equiv Fe^{W}OPb^{+}$ can be almost negligible. However, for the other six HMs, $\equiv Fe^{S}OM^{+}$, and $\equiv Fe^{W}OM^{+}$ were both the main adsorption forms and the contribution of $\equiv Fe^{W}OM^{+}$ was greater than that of $\equiv Fe^{S}OM^{+}$. The above results indicated that the adsorption mechanism of Pb and the other six HMs on the surface of Fh was different, which may be related to the outer electron arrangement of these HMs. Applying the fitting parameters of mono-systems to a mixed system can still achieve good fitting results (Fig. S1†), which indicated that it was feasible to use fitting parameters of mono-systems to describe the adsorption behavior of HMs on the surface of Fh in a mixed system.

3.5 Surface structure of Fh

The surface structure is a significant factor in controlling the properties of minerals, particularly the interfacial chemical reactions occurring at the mineral surfaces. Based on the XRD results from this study (Fig. 1), priority attention should be given to the (103), (112), and (201) facets of Fh. As shown in Fig. 5, the structures of the three aspects are distinct. The side view of the (103) face showed that the hydroxyl group (OH) is exposed at the edge, while the top view showed that the iron atoms were coordinated with four or five oxygens. However, the

Table 1 Modeling parameters for Pb^{2+}, Cu^{2+}, Zn^{2+}, Cd^{2+}, Ni^{2+}, Co^{2+} and Mn^{2+} adsorption on Fh

Site type	Site density (mmol L^{-1})
$\equiv Fe^{s}OH$	0.3675
$\equiv Fe^{w}OH$	14.775

Surface acid–base reactions	Log
$\equiv Fe^{s}OH \leftrightarrow \equiv Fe^{s}O^{-} + H^{+}$	−8.93
$\equiv Fe^{s}OH + H^{+} \leftrightarrow \equiv Fe^{s}OH_2^{+}$	7.29
$\equiv Fe^{w}OH \leftrightarrow \equiv Fe^{w}O^{-} + H^{+}$	−8.93
$\equiv Fe^{w}OH + H^{+} \leftrightarrow \equiv Fe^{w}OH_2^{+}$	7.29

Surface complexation reactions	Log K	Other study	References
$\equiv Fe^{s}OH + Pb^{2+} \leftrightarrow \equiv Fe^{s}OPb^{+} + H^{+}$	6	6.11	33
$\equiv Fe^{w}OH + Pb^{2+} \leftrightarrow \equiv Fe^{w}OPb^{+} + H^{+}$	2	2.49	
$\equiv Fe^{s}OH + Cu^{2+} \leftrightarrow \equiv Fe^{s}OCu^{+} + H^{+}$	2.75	2.89	34
$\equiv Fe^{w}OH + Cu^{2+} \leftrightarrow \equiv Fe^{w}OCu^{+} + H^{+}$	0	—	
$\equiv Fe^{s}OH + Zn^{2+} \leftrightarrow \equiv Fe^{s}OZn^{+} + H^{+}$	1.5		
$\equiv Fe^{w}OH + Zn^{2+} \leftrightarrow \equiv Fe^{w}OZn^{+} + H^{+}$	−1.7		
$\equiv Fe^{s}OH + Cd^{2+} \leftrightarrow \equiv Fe^{s}OCd^{+} + H^{+}$	1	0.47	35
$\equiv Fe^{w}OH + Cd^{2+} \leftrightarrow \equiv Fe^{w}OCd^{+} + H^{+}$	−1.5	−2.9	
$\equiv Fe^{s}OH + Ni^{2+} \leftrightarrow \equiv Fe^{s}ONi^{+} + H^{+}$	0		
$\equiv Fe^{w}OH + Ni^{2+} \leftrightarrow \equiv Fe^{w}ONi^{+} + H^{+}$	−2.5		
$\equiv Fe^{s}OH + Co^{2+} \leftrightarrow \equiv Fe^{s}OCo^{+} + H^{+}$	0	−0.46	36
$\equiv Fe^{w}OH + Co^{2+} \leftrightarrow \equiv Fe^{w}OCo^{+} + H^{+}$	−2.5	−3.01	
$\equiv Fe^{s}OH + Mn^{2+} \leftrightarrow \equiv Fe^{s}OMn^{+} + H^{+}$	−1		
$\equiv Fe^{w}OH + Mn^{2+} \leftrightarrow \equiv Fe^{w}OMn^{+} + H^{+}$	−2.5		

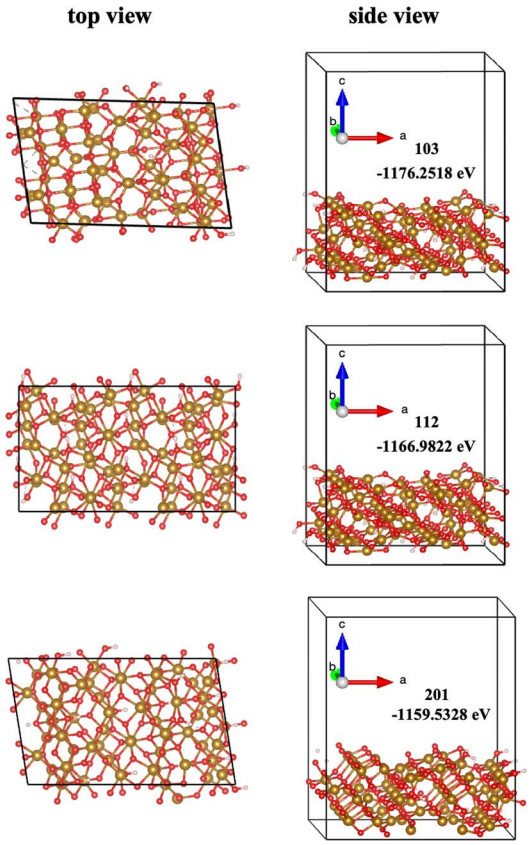

Fig. 5 The surface structure and total energy of different low-index facets of Fh, Fe = orange spheres, O = red spheres, and H = white spheres.

(112) and (201) surfaces exposed not only OH but also Fe atoms coordinated to only three oxygen atoms. Therefore, considering the density of surface-exposed oxygen atoms, it is difficult for cations to adsorb around Fe atoms coordinated with three oxygen atoms on the (112) and (201) facets. Furthermore, the surface energy of the (103) facet was −1176.25 eV, which was much lower than that of the (112) (−1166.98 eV) and (201) (−1159.53 eV) facets. This suggested that the (103) facet would be more stable than others. Therefore, the (103) facet would constitute a more extensive distribution of the Fh surface. The predominant distribution of inert (103) facets for cation adsorption was likely the primary reason limiting the adsorption rate observed with Fh in many previous experimental studies.

The DLM focuses more on describing macroscopic electrical parameters such as interface charge distribution and adsorption kinetics. In contrast, DFT focuses more on calculating microscopic chemical information such as electronic structure, bonding properties, adsorption energy, and molecular configuration. The combination of the two methods can provide a more comprehensive and in-depth understanding on the competitive adsorption mechanism of HMs on the surface of Fh. To understand the differences in adsorption rates of various cations on the Fh surface, we investigated the adsorption energy (E_{ads}) and atomic configurations of cations at seven distinct sites on Fh (103) surface using DFT calculations. At the iron-terminated surface of Fh (103), three distinct iron sites were exposed: a 4-fold coordinated Fe1 site, a 5-fold coordinated Fe2 site, and a 6-fold coordinated Fe3 site (Fig. 6). The likelihood of cation adsorption varied based on the iron sites on the Fh surface. We used Pb^{2+} as a model to study its adsorption properties at different sites on the Fh (103) surface.

As displayed in Fig. 7, the E_{ads} of Pb^{2+} adsorption on the Fh (103) surface ranged from −2.35 to −6.66 eV. This result revealed different possibilities for Pb^{2+} adsorption, depending on the surface iron sites. The two oxygen bridges between Fe2 sites created a favorable coordination environment, allowing for the formation of coordination bonds with Pb^{2+}. This relationship stabilized the electron cloud distribution of Pb^{2+}, enhancing the stability of Pb^{2+} in this position. We also calculated the adsorption capacities and energies of Zn^{2+} and Ni^{2+} at various sites on the Fh (103) surface to investigate differences in cation adsorption rates on the Fh surface (Fig. S2 and S3†). It showed that Zn^{2+} had a more robust adsorption capacity than Ni^{2+} at these sites. By comparing the adsorption energies of the above three cations, we found that Fh had the most muscular adsorption capacity for Pb^{2+}. The Bader charge analysis in Table S1† revealed distinct charge distribution patterns for Pb^{2+}, Zn^{2+}, and Ni^{2+} after adsorption. Pb^{2+} exhibited the highest charge transfer, suggesting stronger coordination with the surface, while Zn^{2+} and Ni^{2+} showed smaller charge transfers, implying weaker interactions. This stronger coordination of Pb^{2+} was further reflected in its higher adsorption energy compared to

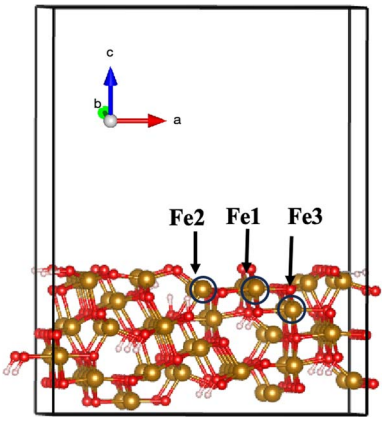

Fig. 6 Schematic illustration of iron sites at the iron-terminated surface of Fh (103).

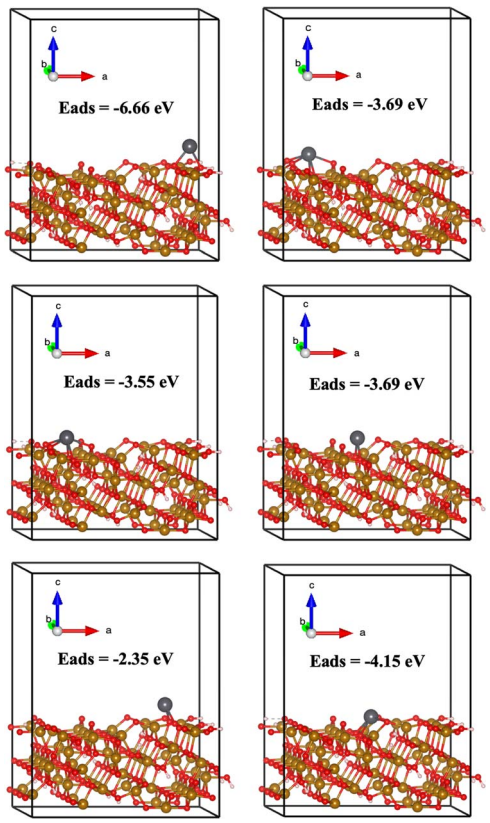

Fig. 7 The E_{ads} and atomic configuration of Pb^{2+} adsorption on different Fh (103) surface sites.

Zn^{2+} and Ni^{2+}. The electron localization function (ELF) analysis in Fig. 8 provided additional support, showing that Pb^{2+} displays more significant electron localization, indicative of stronger coordination bonds. In contrast, Zn^{2+} and Ni^{2+} exhibited weaker electron localization, reinforcing the notion of weaker coordination. Moreover, the bond lengths listed in Table S2† confirm these observations, with Pb^{2+} forming a shorter Pb–O bond (~2.45 Å) compared to Zn–O (2.73 Å) and

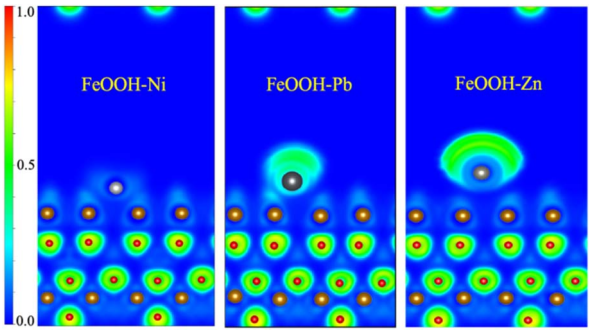

Fig. 8 The ELF of Ni^{2+}, Pb^{2+}, and Zn^{2+} adsorbed on Fh (103).

Ni–O (2.92 Å), further suggesting stronger coordination between Pb^{2+} and the surface oxygen atoms of Fh.[47] We speculate that larger ions tend to form stronger coordination bonds on the Fh surface, particularly when interacting with oxygen-containing functional groups such as hydroxyl groups. These theoretical calculations align closely with our experimental findings, offering robust validation for our conclusions.

4 Conclusion

This study revealed that Fh effectively adsorbs HMs, with the adsorption capacities following the order: Pb^{2+} > Cu^{2+} > Zn^{2+} > Cd^{2+} > Ni^{2+} > Co^{2+} > Mn^{2+}. Pb^{2+} and Cu^{2+} exhibited notably higher adsorption than the other ions, and competitive adsorption occurred in multi-metal systems, as confirmed by adsorption isotherms. The DLM analysis showed that $\equiv Fe^{s}OM$ and $\equiv Fe^{w}OM$ were the predominant adsorption sites for most HMs, while Pb^{2+} predominantly adsorbed *via* $\equiv Fe^{s}OPb$. The DFT calculations further highlighted the role of surface iron site distribution on Fh, showing that larger metal ions like Pb^{2+} form stronger coordination bonds with hydroxyl groups on the Fh surface. These interactions lead to distinct adsorption behavior, particularly in comparison to smaller ions. Overall, the findings underscore the importance of surface iron site distribution and ion size in controlling the adsorption processes, providing valuable insights for better understanding and managing the environmental behavior of HMs.

Data availability

Data will be made available on request.

Author contributions

Bihong He: writing the original draft, project administration, investigation, and funding acquisition. Wentao Zhang: writing – review & editing, supervision, funding acquisition. Yanan Diao: data curation and validation. Shangchen Sun: data curation and validation. Yonghe Zhang: writing – review & editing. Wenqing Zhao: data curation and validation. Fei Wen: data curation and validation. Guangrui Yang: writing – reviewing & editing.

Conflicts of interest

There are no conflicts to declare.

Acknowledgements

Financial supports from National Natural Science Foundation of China (Grant No. 42302190), Natural Science Foundation of Gansu Province (Grant No. 24JRRA093), Innovation Fund Project of Colleges and Universities in Gansu Province (Grant No. 2024A-263), Major Science and Technology Projects of Lanzhou Resources & Environment Voc-Tech University (Grant No. X2022ZD-06), Science and Technology Plan Project of Lanzhou City (Grant No. 2022-2-92).

References

1 X. Dai, L. Feng, X. Ma, *et al.*, Concentration Level of Heavy Metals in Wheat Grains and the Health Risk Assessment to Local Inhabitants from Baiyin, Gansu, China, *Adv. Mater. Res.*, 2012, **518–523**, 951–956.
2 S.-K. Jeon, M. J. Kwon, J.-S. Yang, *et al.*, Identifying the source of Zn in soils around a Zn smelter using Pb isotope ratios and mineralogical analysis, *Sci. Total Environ.*, 2017, **601–602**, 66–72.
3 B. Liu, S. Ai, W. Zhang, *et al.*, Assessment of the bioavailability, bioaccessibility and transfer of heavy metals in the soil-grain-human systems near a mining and smelting area in NW China, *Sci. Total Environ.*, 2017, **609**, 822–829.
4 X. Gou, Y. Li and G. Wang, Heavy metal concentrations and correlations in rain-fed farm soils of Sifangwu village, central Gansu Province, China, *Land Degrad. Dev.*, 2007, **18**, 77–88.
5 H. Li, J. Yao, N. Min, *et al.*, Comprehensive assessment of environmental and health risks of metal(loid)s pollution from non-ferrous metal mining and smelting activities, *J. Cleaner Prod.*, 2022, **375**, 134049.
6 H. Mukai, N. Furuta, T. Fujii, *et al.*, Characterization of sources of lead in the urban air of Asia using ratios of stable lead isotopes, *Environ. Sci. Technol.*, 1993, **27**, 1347–1356.
7 H. Mukai, A. Tanaka, T. Fujii, *et al.*, Lead isotope ratios of airborne particulate matter as tracers of long-range transport of air pollutants around Japan, *J. Geophys. Res.:Atmos.*, 1994, **99**, 3717–3726.
8 H. Mukai, A. Tanaka, T. Fujii, *et al.*, Regional Characteristics of Sulfur and Lead Isotope Ratios in the Atmosphere at Several Chinese Urban Sites, *Environ. Sci. Technol.*, 2001, **35**, 1064–1071.
9 H. Wen, Y. Zhang, C. Cloquet, *et al.*, Tracing sources of pollution in soils from the Jinding Pb–Zn mining district in China using cadmium and lead isotopes, *Appl. Geochemistry*, 2015, **52**, 147–154.
10 H. Zhao, B. Xia, C. Fan, *et al.*, Human health risk from soil heavy metal contamination under different land uses near Dabaoshan Mine, Southern China, *Sci. Total Environ.*, 2012, **417–418**, 45–54.
11 C. Duan, L. Fang, C. Yang, *et al.*, Reveal the response of enzyme activities to heavy metals through in situ zymography, *Ecotoxicol. Environ. Saf.*, 2018, **156**, 106–115.
12 B. He, W. Wang, R. Geng, *et al.*, Exploring the fate of heavy metals from mining and smelting activities in soil-crop system in Baiyin, NW China, *Ecotoxicol. Environ. Saf.*, 2021, **207**, 111234.
13 B. He, X. Zhao, P. Li, *et al.*, Lead isotopic fingerprinting as a tracer to identify the pollution sources of heavy metals in the southeastern zone of Baiyin, China, *Sci. Total Environ.*, 2019, **660**, 348–357.
14 X. Zhao, B. He, H. Wu, *et al.*, A comprehensive investigation of hazardous elements contamination in mining and smelting-impacted soils and sediments, *Ecotoxicol. Environ. Saf.*, 2020, **192**, 110320.
15 X. Hu, Y. Sun, Z. Ding, *et al.*, Lead contamination and transfer in urban environmental compartments analyzed by lead levels and isotopic compositions, *Environ. Pollut.*, 2014, **187**, 42–48.
16 P. Sipos, A. Tóth, V. K. Kis, *et al.*, Partition of Cd, Cu, Pb and Zn among mineral particles during their sorption in soils, *J. Soils Sediments*, 2019, **19**, 1775–1787.
17 B. He, W. Xie, Y. Wang, *et al.*, Distribution Characteristics of Heavy Metals and Pb Isotope in Profile Soils from a Mining and Smelting Area in Northwestern China, *Adsorpt. Sci. Technol.*, 2021, **2021**, 5913182.
18 F. Li, C. Liu, Y. Yang, *et al.*, Natural and anthropogenic lead in soils and vegetables around Guiyang city, southwest China: A Pb isotopic approach, *Sci. Total Environ.*, 2012, **431**, 339–347.
19 S. P. McGrath, F. J. Zhao and E. Lombi, Plant and rhizosphere processes involved in phytoremediation of metal-contaminated soils, *Plant Soil*, 2001, **232**, 207–214.
20 P. Mirmiran, N. Noori, M. B. Zavareh, *et al.*, Fruit and vegetable consumption and risk factors for cardiovascular disease, *Metabolism*, 2009, **58**, 460–468.
21 A. Åkesson, T. Lundh, M. Vahter, *et al.*, Tubular and Glomerular Kidney Effects in Swedish Women with Low Environmental Cadmium Exposure, *Environ. Health Perspect.*, 2005, **113**, 1627–1631.
22 A. Engström, K. Michaëlsson, Y. Suwazono, *et al.*, Long-term cadmium exposure and the association with bone mineral density and fractures in a population-based study among women, *J. Bone Miner. Res.*, 2011, **26**, 486–495.
23 C. M. Gallagher, J. J. Chen and J. S. Kovach, Environmental cadmium and breast cancer risk, *Aging*, 2010, **2**(11), 804–814.
24 L. D. K. Thomas, K. Michaëlsson, B. Julin, *et al.*, Dietary cadmium exposure and fracture incidence among men: A population-based prospective cohort study, *J. Bone Miner. Res.*, 2011, **26**, 1601–1608.
25 H. A. Godwin, The biological chemistry of lead, *Curr. Opin. Chem. Biol.*, 2001, **5**, 223–227.
26 T. E. Graedel, D. van Beers, M. Bertram, *et al.*, The Multilevel Cycle of Anthropogenic Zinc, *J. Ind. Ecol.*, 2005, **9**(3), 67–90.
27 X. Wang, K. Yang, S. Sun, *et al.*, The structure and composition of ferrihydrite and its environmental geochemical behaviors, *Earth Sci. Front.*, 2011, **18**, 339–347.

28 L. Tian, Y. Liang, Y. Lu, *et al.*, Pb(II) and Cu(II) Adsorption and Desorption Kinetics on Ferrihydrite with Different Morphologies, *Soil Sci. Soc. Am. J.*, 2018, **82**, 96–105.
29 R. Yang, J. Tao, Q. Huang, *et al.*, Co-adsorption of Cd(II) and Sb(III) by ferrihydrite: a combined XPS and ITC study, *J. Soils Sediments*, 2019, **19**, 1319–1327.
30 W. Yang, Y. Zhang, J. Zheng, *et al.*, Migration of spent grain-modified colloidal ferrihydrite: Implications for the in situ stabilization of arsenic, lead, and cadmium in co-contaminated soil, *Chemosphere*, 2023, **344**, 140310.
31 H. A. Elliott, M. R. Liberati and C. P. Huang, Competitive Adsorption of Heavy Metals by Soils, *J. Environ. Qual.*, 1986, **15**, 214–219.
32 U. K. Saha, S. Taniguchi and K. Sakurai, Simultaneous Adsorption of Cadmium, Zinc, and Lead on Hydroxyaluminum- and Hydroxyaluminosilicate-Montmorillonite Complexes, *Soil Sci. Soc. Am. J.*, 2002, **66**, 117–128.
33 T. J. Reich, S. Das, C. M. Koretsky, *et al.*, Surface complexation modeling of Pb(II) adsorption on mixtures of hydrous ferric oxide, quartz and kaolinite, *Chem. Geol.*, 2010, **275**, 262–271.
34 T. J. Lund, C. M. Koretsky, C. J. Landry, *et al.*, Surface complexation modeling of Cu(II) adsorption on mixtures of hydrous ferric oxide and kaolinite, *Geochem. Trans.*, 2008, **9**(9), 1–16.
35 M. S. Schaller, C. M. Koretsky, T. J. Lund, *et al.*, Surface complexation modeling of Cd(II) adsorption on mixtures of hydrous ferric oxide, quartz and kaolinite, *J. Colloid Interface Sci.*, 2009, **339**, 302–309.
36 C. J. Landry, C. M. Koretsky, T. J. Lund, *et al.*, Surface complexation modeling of Co(II) adsorption on mixtures of hydrous ferric oxide, quartz and kaolinite, *Geochim. Cosmochim. Acta*, 2009, **73**, 3723–3737.
37 N. Pinney, J. D. Kubicki, D. S. Middlemiss, *et al.*, Density Functional Theory Study of Ferrihydrite and Related Fe-Oxyhydroxides, *Chem. Mater.*, 2009, **21**, 5727–5742.
38 E. Van Eynde, T. Hiemstra and R. N. J. Comans, Interaction of Zn with ferrihydrite and its cooperative binding in the presence of PO_4, *Geochim. Cosmochim. Acta*, 2022, **320**, 223–237.
39 U. Schwertmann and R. M. Cornell, *Iron oxides in the laboratory: preparation and characterization*, John Wiley & Sons, 2008.
40 J. P. Gustafsson, *Visual MINTEQ Version 3.1*, 2021, **http://vminteq.com**.
41 G. Kresse and J. Furthmüller, Efficiency of ab-initio total energy calculations for metals and semiconductors using a plane-wave basis set, *Comput. Mater. Sci.*, 1996, **6**, 15–50.
42 J. P. Perdew, J. A. Chevary, S. H. Vosko, *et al.*, Atoms, molecules, solids, and surfaces: Applications of the generalized gradient approximation for exchange and correlation, *Phys. Rev. B: Condens. Matter Mater. Phys.*, 1992, **46**, 6671–6687.
43 P. E. Blöchl, Projector augmented-wave method, *Phys. Rev. B: Condens. Matter Mater. Phys.*, 1994, **50**, 17953–17979.
44 S. Grimme, J. Antony, S. Ehrlich, *et al.*, A consistent and accurate ab initio parametrization of density functional dispersion correction (DFT-D) for the 94 elements H-Pu, *J. Chem. Phys.*, 2010, **132**, 154104.
45 M. Cococcioni and S. de Gironcoli, Linear response approach to the calculation of the effective interaction parameters in the LDA+U method, *Phys. Rev. B: Condens. Matter Mater. Phys.*, 2005, **71**, 035105.
46 R. F. W. Bader, Atoms in molecules, *Acc. Chem. Res.*, 1985, **18**, 9–15.
47 Q. Li, W. Shi and Q. Yang, Polarization induced covalent bonding: A new force of heavy metal adsorption on charged particle surface, *J. Hazard. Mater.*, 2021, **412**, 125168.